Verification and validation of large eddy simulations of turbulent cavitating flow around two marine propellers with emphasis on the skew angle effects

Yun Long[a,b], Chengzao Han[a,b], Bin Ji[a,*], Xinping Long[a,b], Yiwei Wang[c]

[a] State Key Lab of Water Resources and Hydropower Engineering Science, School of Power and Mechanical Engineering, Wuhan University, Wuhan 430072, China
[b] Key Lab of Jet Theory and New Technology of Hubei Province, Wuhan University, Wuhan 430072, China
[c] Key Laboratory for Mechanics in Fluid Solid Coupling Systems, Institute of Mechanics, Chinese Academy of Sciences, Beijing 100190, China

ARTICLE INFO

ABSTRACT

Large eddy simulation (LES) was used to simulate turbulent cavitating flow around a conventional marine propeller (CP) and a highly skewed marine propeller (HSP) with emphasis on the skew angles effects. The LES verification and validation (V&V) analysis was carried out with cavitation influence on the flow structures. The current numerical results demonstrate that LES can give excellent predictions of the transient complex cavitating flows around a CP and a HSP with the numerical results agreeing well with experimental data. This study applies the LES V&V to the cavitating flow around two propellers with a simplified three-equation method. The results show that the LES errors for HSP are smaller than for CP, which is mainly resulted by more skewed blade of HSP than CP. In addition, the cavitation-vortex interactions around the propellers were studied using the relative vorticity transport equation. The results indicate that both the baroclinic torque term and the Coriolis force term have important influences on the vorticity generation and transport in the cavity closure region. Further analyses indicate that most of the important flow structures including the tip vortex, leading edge vortex, trailing vortex and internal jet are reproduced by the current LES simulations. Due to the different geometry features (less skewed blade of CP than HSP), significantly more intense and violent vortical structures and cavitation phenomena are observed on the CP than on the HSP.

1. Introduction

Propeller cavitation has been a key issue in cavitation research for a long time due to the distorted geometry and complex flow mechanisms [1–3]. Cavitation is inevitable on propellers nowadays as ship loads and speeds rapidly increase. The cavitation causes harmful noise, material erosion and performance reductions that can pose a major threat to the safety and stability of the ship. Thus, propeller cavitation is a significant research topic that should be studied further.

Experimental measurements have been used to study propeller cavitation, but such studies still can't fully keep up with the need of practical engineering designs due to many limitations and the limited available data [4]. Thus, many researchers have preferred to use numerical methods to study cavitating flows around propellers. Rhee et al. [5] used an unstructured grid to simulate the propeller open water and cavitation performances. The overall predicted cavity shapes matched the experimental data, while the predicted tip vortex cavitation needed improvement. Takashi and Jun [6] used a simple surface panel method to study steady and unsteady cavitating flows with non-uniform

inflows. The cavity patterns were approximately reproduced for a conventional propeller (CP) and a highly skewed propeller (HSP) on the SEIUN-MARU ship but with the need for significant improvements in the cavitation prediction accuracy. Lindau et al. [7] used Reynolds-averaged Navier-Stokes (RANS) to predict the propeller thrust and torque breakdown due to cavitation. The predicted performance breakdown and the critical cavitation number agreed well with experimental data. Ji et al. [8–10] simulated unsteady cavitation with a non-uniform inlet boundary for a HSP and a CP with reasonable predictions of the relationship between the cavitation and the pressure fluctuations. Regener et al. [11] compared the influence of a nominal wake at model scale and an effective wake at full scale on propeller cavitation predictions. Their results showed that the model scale at nominal wake underpredicted the cavitation and pressure fluctuations. Many other researchers [12–14] have demonstrated that numerical methods can be used to predict the basic propeller cavity shape and area.

Although numerical simulations have improved in recent years, numerous investigations are still limited to predictions of the propeller

---

performance and cavitation patterns. Current investigations of the cavitation mechanisms and cavitation influence on the local flow field around a propeller are still limited with Large eddy simulation (LES) due to the high mesh requirement and calculation consuming. LES has been widely used for fundamental cavitation research [1,15,16], and it is also a promising choice to improve simulation accuracies and propeller cavitation studies. Bensow and Bark [17,18] used LES to model propeller cavitating flows with uniform and artificial wake inflows with reasonable agreement between predicted and measured cavity patterns and good predictions of the internal jet. Lu et al. [19] showed that LES was superior to RANS for predicting complex propeller cavitation structures. The LES method captured the complex vortical structures and vortex interactions [20]. Yu et al. [21] used LES to simulate unsteady cavitating flows around a HSP in a non-uniform wake with the results showing that cavitation was more easily induced in the vortex tube. Although, the LES method has been used in propeller cavitation research with excellent results, there are only a few such studies due to the rigorous mesh and calculational requirements. Thus, more LES investigations with quantitative accuracy demonstrations are needed.

The high accuracy and fidelity of the LES method has been widely recognized by various researchers, but there are few studies giving quantitative accuracy data in the published literature. Mesh independence studies and accuracy investigations still rely on qualitative comparisons with experimental data. Rigorous studies are urgently needed to present LES accuracy data. Analyses with quantitative accuracy data are useful to demonstrate the reliability of numerical results for complex cavitating flow, when there are few experimental data to verify the simulation results. Verification and validation (V&V) is a procedure to assess calculation accuracies, including the evaluations of the physical models and numerical results [22,23]. The American Society of Mechanical Engineers defines verification as determining the accuracy of the numerical solution process and validation as verifying that the physical models accurately reflect the real world physics [23]. Unlike the widely used RANS V&V [23], LES V&V is an important but challenging issue requiring further study. Freitag and Klein [24], Klein [25] and Xing [26] proposed useful methods for LES V&V by quantifying the LES errors. The LES V&V method proposed by Xing [26] and improved by Dutta and Xing [27,28] is one of the most comprehensive methods for promoting LES V&V studies. Up to now, only Long et al. [15,29] has applied LES V&V to unsteady hydrofoil cavitation, while no published studies claimed to apply LES V&V to propeller cavitation. In this study, LES V&V is applied to propeller cavitation using the simplified three-equation method to demonstrate the calculation accuracy with quantitative data.

This study extends these previous studies with LES V&V of turbulent cavitating flows around the CP and HSP with emphasis on the skew angle effects. The LES is coupled with the Zwart et al. cavitation model to model the transient cavitating flow around these two propellers. LES V&V with simplified three-equation are used in propeller cavitation. The LES error distributions and the influence of the cavitation on the LES errors are studied using ten refined structured meshes (five meshes for the CP and five meshes for the HSP). In addition, the LES is also used to study the propeller cavitation-vortex interactions, vortical structures

and the side-entrant jet.

2. Governing equations

The liquid/vapor two-phase flow was predicted numerically by solving the conservation equations for mass and momentum with a transport equation for the vapor volume fraction. Detailed information is given below.

2.1. Conservation equations

The mass and momentum conservation equations for LES are obtained by filtering the time-dependent Navier-Stokes equations. The filtered variable (denoted by an overbar) is written as

$$\overline{\phi}(x) = \int_D \phi(x') G(x, x') dx' \tag{1}$$

where D and G denote the fluid domain and filter function.

In this study, the finite-volume discretization itself implicitly provides the filtering operation as

$$\widetilde{\phi}(x) = \frac{1}{V} \int_v \phi(x') dx', \, x' \in v \tag{2}$$

where V is the volume of a computational cell. The filter function implied here is

$$G(x, x') = \begin{cases} 1/V, \, x' \in v \\ 0, \, x' \in otherwise \end{cases} \tag{3}$$

After filtering, the mass and momentum conservation equations for LES are

$$\frac{\partial \rho_m}{\partial t} + \frac{\partial (\rho_m \widetilde{u}_j)}{\partial x_j} = 0 \tag{4}$$

$$\frac{\partial (\rho_m \widetilde{u}_i)}{\partial t} + \frac{\partial (\rho_m \widetilde{u}_i \widetilde{u}_j)}{\partial x_j} = -\frac{\partial \widetilde{p_m}}{\partial x_i} + \frac{\partial}{\partial x_j}\left(\mu_m \frac{\partial \widetilde{u}_i}{\partial x_j}\right) - \frac{\partial (\tau_{ij})}{\partial x_j} \tag{5}$$

where p_m is the mixture pressure, and ρ_m and μ_m are the mixture density and dynamic viscosity. τ_{ij} are the subgrid-scale (SGS) stresses defined by

$$\tau_{ij} = \rho_m (\widetilde{u_i u_j} - \widetilde{u}_i \widetilde{u}_j) \tag{6}$$

The large scale eddies in the turbulent flow are solved directly while the small scale eddies are modeled by appropriate SGS models. An eddy viscosity approach is used by scaling the strain rate tensor, $\widetilde{S}_{ij}$, as,

$$\tau_{ij} - \frac{1}{3}\tau_{kk}\delta_{ij} = -2\mu_{sgs}\widetilde{S}_{ij} \tag{7}$$

$$\widetilde{S}_{ij} = \frac{1}{2}\left(\frac{\partial \widetilde{u}_i}{\partial x_j} + \frac{\partial \widetilde{u}_j}{\partial x_i}\right) \tag{8}$$

where ν_{sgs} represents the SGS turbulent viscosity. The isotropic part of τ_{ij}, i.e. τ_{kk} is not modeled, but is added to the filtered static pressure. The Smagorinsky model [30] was used here to calculate the SGS turbulent viscosity in this study to model the cavitating flow around the

propeller. The Smagorinsky model is an algebraic model for the SGS viscosity which can be expressed as,

$$\mu_{\text{sgs}} = \rho_{\text{m}} L_{\text{s}}^2 \sqrt{2\widetilde{S_{ij}}\widetilde{S_{ij}}} \tag{9}$$

$$L_{\text{s}} = C_s \Delta \tag{10}$$

where C_s is the Smagorinsky constant equal to 0.1. Δ is the filter width. A viscosity damping function is used close to the walls in place of Eq. (10) with $L_{\text{s}} = \min(\kappa y_{\text{wall}}, C_s \Delta)$, where κ is the von Kármán constant and y_{wall} is the distance to the closest wall.

The investigations by Hadjadj et al. [31], Ben-Nasr et al. [32] and Rieth et al. [33] showed that different SGS models behaved differently for the flows in the channel and over a flat plate, but only much few differences were observed among different SGS models. In addition, the curved wall effects might influence the validation of SGS models [34]. As for the Smagorinsky model [30] adopted in this study, the short-coming of this model is that model coefficient C_s might not be a universal constant suitable for all cases. However it should be noted that even though the weakness of the Smagorinsky model exists, it's still a good choice to model the cavitating flow with good agreement with the experiment in cavitation simulation [15,16,35].

The two-phase cavitating flow was modeled using the transport equation with a homogeneous assumption, and the liquid and vapor phases are assumed to be incompressible. This method is compatible with LES. The distributions of the two phases were specified by the volume fraction. The transport equation model and the mixture quantities in Eqs. (4) and (5) scaled by the vapor volume fraction, α_v, can be expressed as,

$$\frac{\partial \alpha_l}{\partial t} + \frac{\partial (\alpha_l \widetilde{u}_j)}{\partial x_j} = \frac{\dot{m}}{\rho_l} \tag{11}$$

$$\rho_{\text{m}} = \rho_v \alpha_v + \rho_l (1 - \alpha_v) \tag{12}$$

$$\mu_{\text{m}} = \mu_v \alpha_v + \mu_l (1 - \alpha_v) \tag{13}$$

where subscripts l and v refer to the water and vapor phases. The source term, $\dot{m}$, on the right side of Eq. (11) is the mass transfer between the liquid and vapor phases. Various methods have been proposed to calculate this source terms [36–38]. The Zwart et al. cavitation model [38], which has been widely validated in simulations of cavitating flows [15,29,39], was used in this study. The mass transfer in the Zwart et al. cavitation model was calculated as,

$$\dot{m} = \frac{3\alpha_v \rho_v}{R_{\text{B}}} \sqrt{\frac{2}{3} \frac{|p_v - p_{\text{m}}|}{\rho_l}} \tag{14}$$

where R_{B} is the bubble diameter, which was set to 10^{-6} m. Eq. (11) was modified for the condensation and vaporization processes due to the large differences in the mass transfer rates for condensation and vaporization as,

$$\dot{m}^+ = C_{\text{cond}} \frac{3\alpha_v \rho_v}{R_{\text{B}}} \sqrt{\frac{2}{3} \frac{\max(p_{\text{m}} - p_v, 0)}{\rho_l}} \tag{15}$$

$$\dot{m}^- = C_{\text{vap}} \frac{3\alpha_{\text{nuc}}(1 - \alpha_v)\rho_v}{R_{\text{B}}} \sqrt{\frac{2}{3} \frac{\max(p_v - p_{\text{m}}, 0)}{\rho_l}} \tag{16}$$

where α_{nuc} denotes the nucleation site volume fraction which was set to 5×10^{-4}. C_{vap} and C_{cond} are the empirical constants for vaporization and condensation, which were set to 50 and 0.01 recommended by Zwart et al. [38]. These constants have been shown to predict complex cavitating flows with good agreement with the experiments [14,15,38-40].

2.2. Relative vorticity transport equation

The relative vorticity transport equation in cylindrical coordinates

was used to study the influence of the propeller cavitation on the vorticity in this study. The relative vorticity transport equation is the curl of the incompressible Navier-Stokes equations for propeller cavitation with a constant rotation speed [39],

$$\frac{\partial \vec{\Omega}_{rel}}{\partial t} = \left(\vec{\Omega}_{rel} \cdot \nabla\right) \vec{U}_{rel} - \vec{\Omega}_{rel}\left(\nabla \cdot \vec{U}_{rel}\right) + \frac{1}{\rho_{\text{m}}^2} \nabla \rho_{\text{m}} \times \nabla p_{\text{m}} - 2\nabla \times \left(\vec{\omega} \times \vec{U}_{rel}\right)$$
$$+ \nu \nabla^2 \vec{\Omega}_{rel} \tag{17}$$

where subscript rel indicates the variable in cylindrical coordinate, $\vec{\Omega}_{rel}$ and $\vec{U}_{rel}$ denote the relative vorticity and relative velocity, and ν is the kinematic viscosity and ω is the propeller rotational speed. The term on the left side is the material derivative of the relative vorticity. The first term on the right side is the relative vortex stretching term due to the vortex stretching and tilting induced by the velocity gradients. The second term on the right is the relative vortex dilatation term due to the volumetric expansion or contraction. The third term on the right denotes the baroclinic torque term which results from the misalignment of the pressure gradient and the mixture density gradient. The fourth term is the Coriolis force term due to the propeller rotation. The last term denotes the viscous diffusion effect which in high Reynolds flows has little effect on the vorticity transport.

3. LES V&V methods for propeller cavitation flows

LES V&V in hydrofoil cavitating flows has been studied by our previous investigations [15,29] with the LES V&V method for propeller cavitation derived here in a similar way. The total error between the LES and the exact numerical solution can be mainly decomposed into the numerical error and modeling error [15,28]. However the exact numerical solution is usually difficult to solve for cavitation calculation, so it is replaced by the numerical benchmark. The numerical benchmark denotes the high accuracy numerical result and it should be accepted by most of researchers. Then the errors between the numerical benchmark and the exact numerical solution are neglected, and the numerical error and modeling error are the main components of LES errors. For the Mesh 1 shown in Table 1, the LES errors derived from the H2-5 LES V&V method by Xing [26] and our cavitation studies [15,29] can be expressed as,

$$S_1 - S_C = c_N (h^*)^{p_N} + c_M \Delta^{p_M} \tag{18}$$

where S_1 is the solution of a variable for Mesh 1, S_C is the numerical benchmark, c_N and c_M are the numerical error coefficient and the modeling error coefficient, p_N and p_M are the orders of accuracy for the numerical error and the modeling error, and h^* is the square root of the product of the local mesh size and the time step. The first term on the right side of Eq. (18) is the numerical error and the second is the modeling error for Mesh 1. The five-equation LES V&V method requires five systematically refined meshes with transient calculations to solve for the five unknowns (S_C, c_N, c_M, p_N and p_M),

$$S_1 - S_C = c_N (h^*)^{p_N} + c_M \Delta^{p_M} \tag{19}$$

$$S_2 - S_C = c_N (rh^*)^{p_N} + c_M (r\Delta)^{p_M} \tag{20}$$

$$S_3 - S_C = c_N (r^2 h^*)^{p_N} + c_M (r^2 \Delta)^{p_M} \tag{21}$$

Table 1.
Mesh information and setup for HSP

Mesh	Number of elements	Time-step/s
1	29 886 818	1.0599×10^{-4}
2	17 232 399	1.27188×10^{-4}
3	9 9295 26	1.52625×10^{-4}
4	5 723 192	1.8315×10^{-4}
5	3 300 400	2.1978×10^{-4}

Table 2.
Mesh information and setup for CP

Mesh	Number of elements	Time-step/s
6	26 737 004	1.27817×10^{-4}
7	15 459 770	1.5338×10^{-4}
8	8 938 695	1.84056×10^{-4}
9	5 167 882	2.20868×10^{-4}
10	2 991 944	2.65041×10^{-4}

Table 3.
Main Specifications for the HSP and CP

Propeller	HSP	CP
Number of blades, Z	5	5
Diameter, D (mm)	220	220.95
Pitch ratio (at $0.35D$)	0.944	0.95
Skew angle (degree)	45	10.5
Expanded area ratio	0.7	0.65
Rotation speed, n (rps)	17.5	17.15

$$S_4 - S_C = c_N (r^3 h^*)^{p_N} + c_M (r^3 \Delta)^{p_M} \tag{22}$$

$$S_5 - S_C = c_N (r^4 h^*)^{p_N} + c_M (r^4 \Delta)^{p_M} \tag{23}$$

where r is the time step and mesh refinement ratio which was 1.2 in this study. The time-consuming solution procedure for the five-equation method is very expensive and unrealistic, so the five-equation method was simplified to the three-equation method after obtaining reasonable values for p_N and p_M. The three-equation method can then be expressed as,

$$S_1 - S_C = c_N (h^*)^{p_N} + c_M \Delta^{p_M} \tag{24}$$

$$S_2 - S_C = c_N (rh^*)^{p_N} + c_M (r\Delta)^{p_M} \tag{25}$$

$$S_3 - S_C = c_N (r^2 h^*)^{p_N} + c_M (r^2 \Delta)^{p_M} \tag{26}$$

Five systematic refined meshes are constructed as shown in Table 1 for HSP and Table 2 for CP to do the transient calculations. The total cavity volume was used as the target to solve the five highly non-linear equations, Eqs. (19)-(23). The resolved values of p_N and p_M were then found to be 1.48 and 1.37 for HSP and 1.32 and 1.21 for CP. Then, the LES errors were calculated using the simplified three-equation method.

In general, based on the existing researches [22,23,26,28] and our previous studies [15,29] on LES V&V, the recommended choice of the refinement ratio is in the range 1 to 2. Too large refinement ratio will lead to unbearable computational consuming, while too small ratio might make the magnitude of iterative error and LES errors locating on the same level. It should be noted that all calculations in this study have ensured that the iterative error is two orders of magnitude smaller than LES errors, and it is usually neglected when discussing LES errors. So within the current calculation capacity, larger refinement ratio is chosen for three equations. Mesh triplets 1-3-5 and 6-8-10 are used to apply in the simplified three-equation method for HSP and CP respectively.

4. Propeller geometry, computational setup and mesh information

The marine propellers used in this study are model propellers for the CP and HSP used in the "SEIUN-MARU" ship and tested by Kurobe et al. [41]. Fig. 1 shows geometry sketches of the two propellers (HSP and CP). The HSP blades are much more skewed than the CP blades as shown in Fig. 1. The main specifications of the two model propellers are listed in Table 3. Fig. 2 shows the computational domain and boundary conditions for the propeller cavitation calculations. The computational domain was divided into a rotating part and a stationary part connected together by a general grid interface (GGI) interface in ANSYS CFX solver. This treatment has been verified to be useful to balance the calculational accuracy and time consumption [8,10,14,21,39]. The propeller was located in the rotational part with no-slip wall imposed on the blade surface. The outer cylindrical surface of the stationary part was set as a free slip wall.

The non-uniform inlet flow distribution shown in Fig. 3 (a) was used in the calculations with a user defined profile to assign the non-uniform velocity distribution to the boundary inlet. The other flow conditions were set equal to the experimental conditions with the rotational speed set to 17.5 rps for HSP and 17.15 rps for CP. The axial wake fraction (i.e. w in Fig. 3 (a)) based on the experiments is calculated as: w = (V - u_x)/V, where V is the ship velocity, u_x is the axial velocity on the boundary inlet. The advance ratio (J) of propeller is calculated as: J = V / nD, where n is the propeller rotation speed and D is the propeller diameter. The load distribution of propeller will be almost the same between the simulation and experiment if the thrust coefficient between the simulation and experiment is the same. The axial wake distribution and thrust coefficient can be found in experiments, while the advance ratio needs adjustment in simulation to achieve the same thrust coefficient between the simulation and experiment. The average thrust coefficients were found to be 0.201 for HSP and 0.207 for CP by
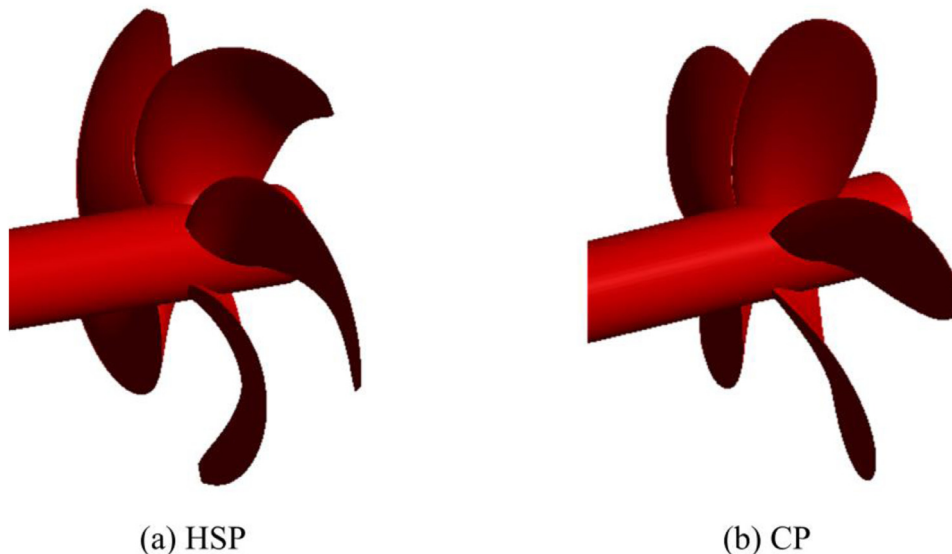

(a) HSP   (b) CP

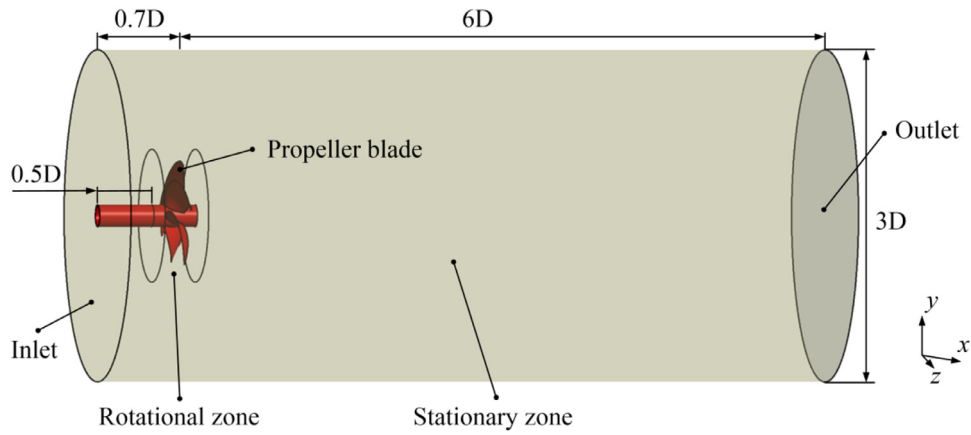**Fig. 1.**. Sketch of the propeller geometries for HSP and CP

Fig. 2.. Computational domain and boundary condition

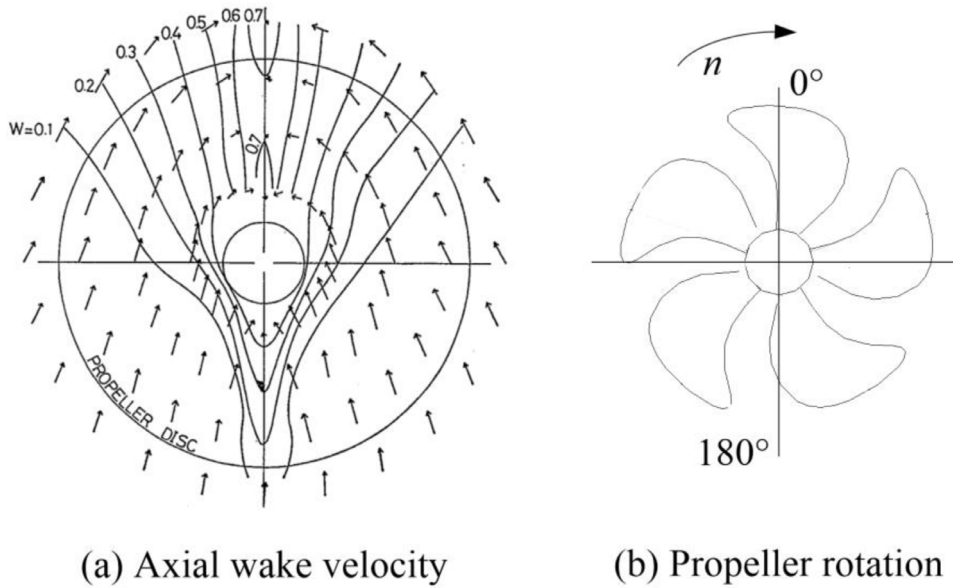(a) Axial wake velocity
(b) Propeller rotation

Fig. 3.. Axial wake velocity distribution [41] and propeller blade angle during rotating
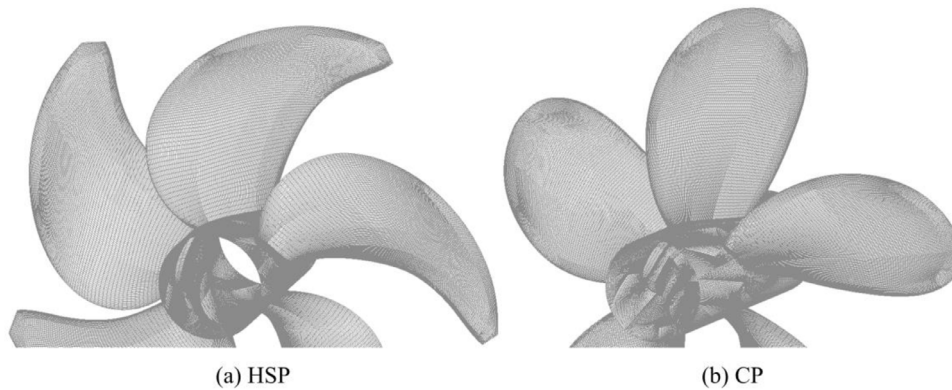

(a) HSP
(b) CP

Fig. 4.. Structured meshes around the HSP for Mesh 5 and CP for Mesh 10

adjusting V and the final advance ratio was set to 0.725 for HSP and 0.727 for CP. The distance between the boundary inlet and propeller was set to 0.7D. We found that a large distance leaded to a uniform velocity distribution in front of the propeller, while a small distance was difficult to obtain convergent results. Thus, 0.7D was adopted based on the pre-calculations. The outlet was set 6D downstream of the propeller with the static pressure arranged on the outlet surface. The pressure on

the boundary outlet is derived from the cavitation number $\sigma = (p-p_v)/(0.5\rho_l n^2 D^2)$, which was 2.99 for HSP and 3.06 for CP according to the experimental data. The blade angle during propeller rotating is shown in Fig. 3 (b).

Five refined structured meshes were generated with the same topology by ANSYS ICEM CFD. The number of elements and the time steps are listed in Table 1 and Table 2. The meshes were refined with a
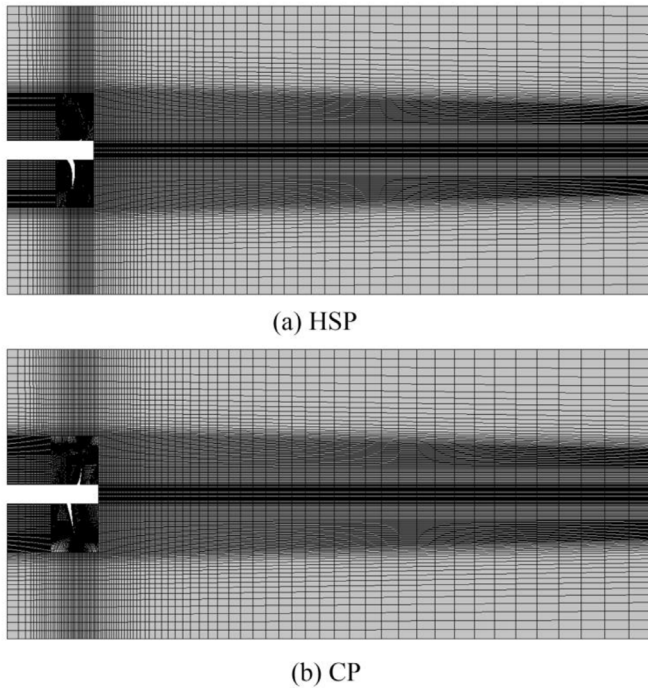
(a) HSP

(b) CP

Fig. 5.. Structured meshes of the fluid domain in *x-y* plane for Mesh 5 of HSP and Mesh 10 of CP
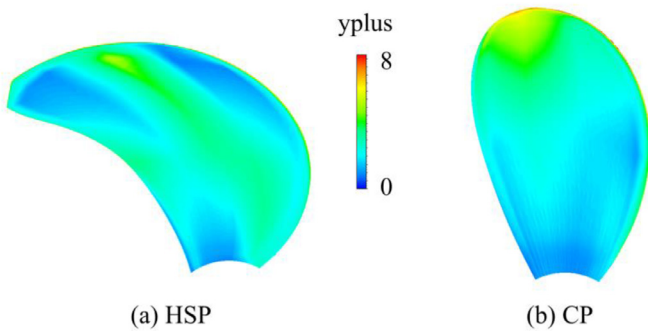

(a) HSP   (b) CP

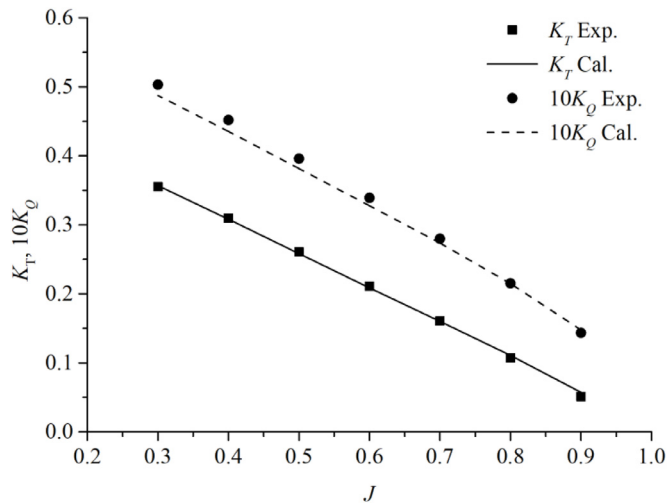**Fig. 6..** Distributions of yplus on the suction surface for HSP and CP

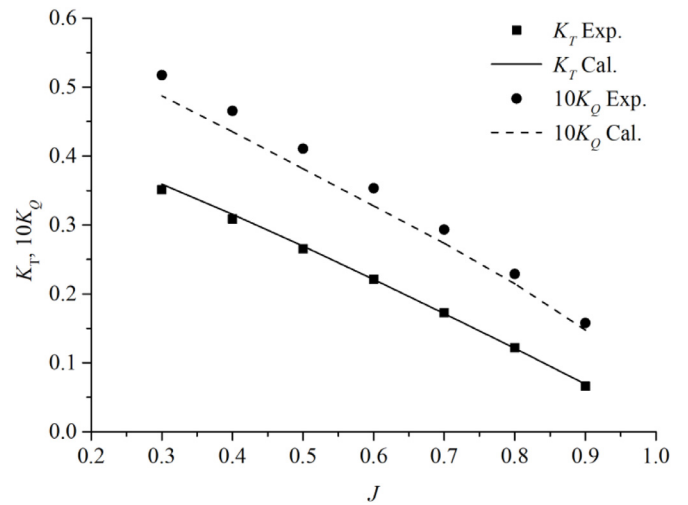**Fig. 7..** Comparison of the measured [41] and predicted open water performance for HSP.

Fig. 8.. Comparison of the measured [41] and predicted open water performance for CP.
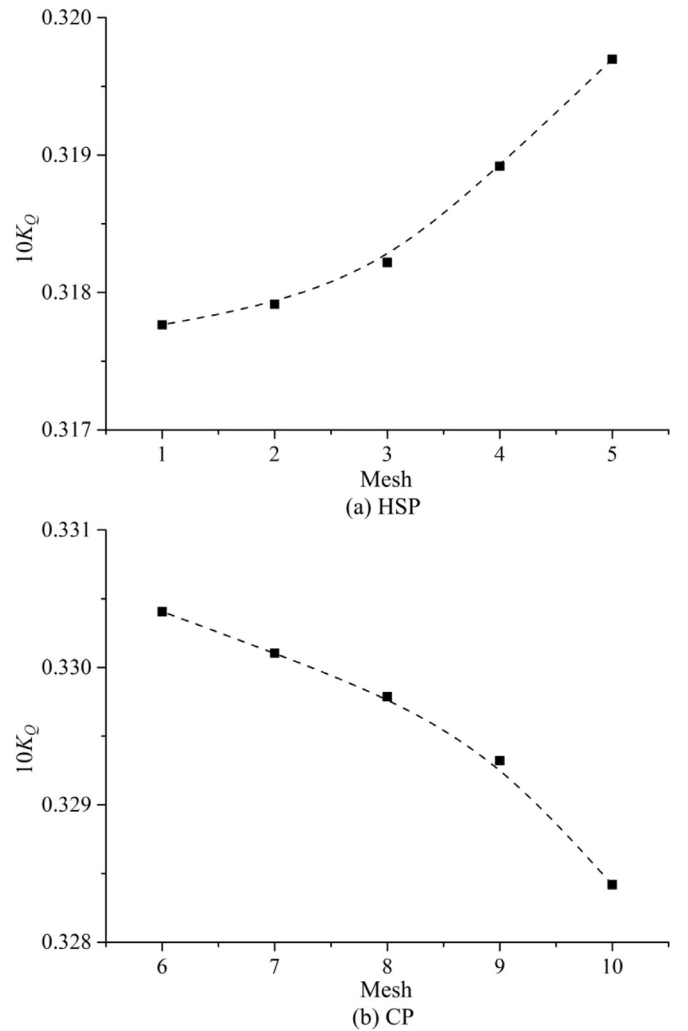

(a) HSP

(b) CP

Fig. 9.. Predicted torque coefficient at $J=0.6$ over five meshes for HSP and CP (Mesh 1 and Mesh 6 are the finest meshes)

constant refinement ratio $r = 1.2$ in the *x, y* and *z* directions. Fig. 4 and Fig. 5 show the structured meshes of the propellers and the fluid domains in the x-y plane for HSP and CP. Fig. 6 shows the distributions of yplus on the suction surface of HSP and CP by Mesh 5 and Mesh 10
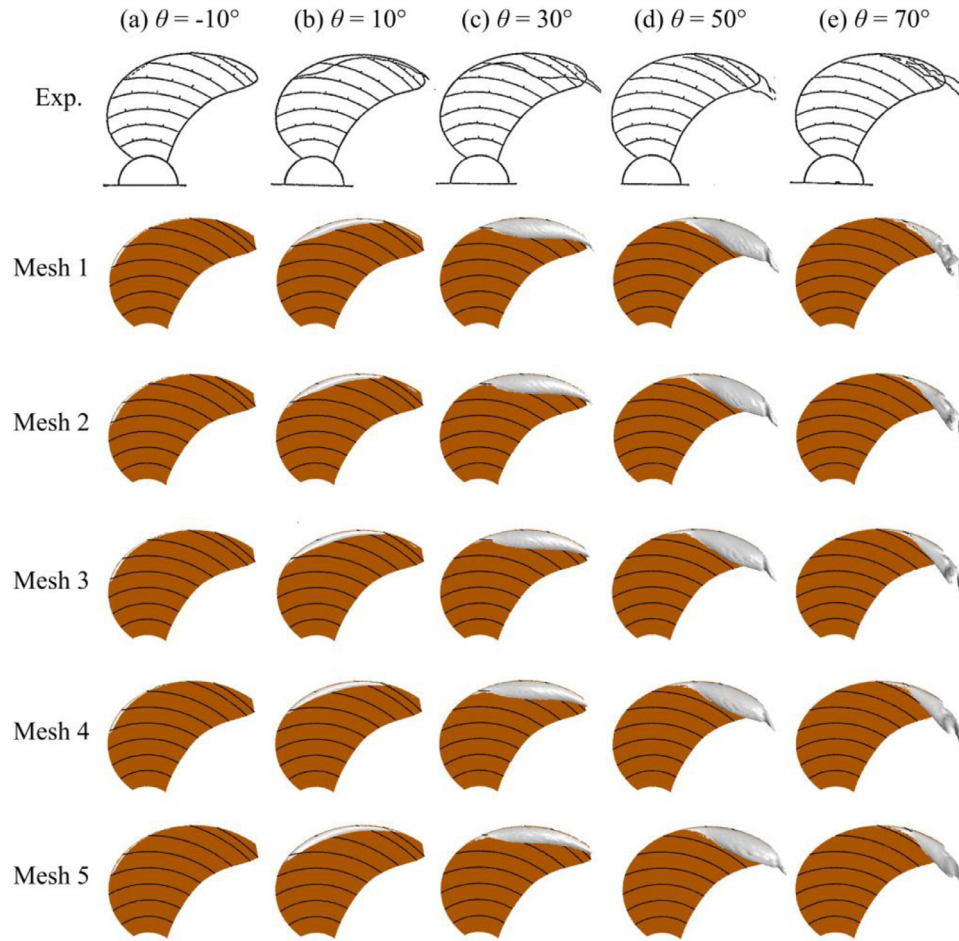
Fig. 10.. Comparison of the predicted and experimental cavity patterns during the propeller rotation for HSP. (Experimental results [41]; predicted results: isosurface of $\alpha_v = 0.1$.)

respectively. The results show that yplus distributions at most of regions are in the range 0 to 4. The definition of yplus is: yplus=$(\Delta y u_\tau)/v$ (Δy denotes the mesh spacing between the wall and the first node away from the wall, u_τ is the friction velocity and ν is the kinematic viscosity). Five meshes for CP and HSP are refined with a constant refinement ratio from the coarsest mesh (Mesh 5 and Mesh 10 for HSP and CP respectively). However, the first mesh spacing to the wall is treated as the same value for all meshes to avoid influencing the calculation of L_S ($L_s = \min(\kappa y_{wall}, C_s \Delta)$) and the application of LES V&V. The minimum skew and orthogonal quality (two quality metrics in ANSYS ICEM CFD) are: 0.3 and 35 for Mesh 5 of HSP; 0.5 and 0.5 for Mesh 10 of CP.

All simulation results in this study were solved by ANSYS CFX. The convergent results of no cavitation were set as the initial flow fields for the transient cavitating flow calculations. The no cavitation results are adopted when 1×10^{-6} RMS residual criterion is achieved. The transient rotor stator model was used in the unsteady calculations. The time-dependent governing equations were discretized in both time and space. The advection term was solved numerically using the bounded central difference scheme. The transient term was solved using the second order backward Euler scheme. The maximum number of inner iterations was 30 per time step with a 5×10^{-4} RMS residual criterion to balance the time consumption and the accuracy. Each transient calculation for all ten meshes (five meshes for HSP and five meshes for CP) ran over 25 propeller revolutions with the statistical data obtained over the final 15 propeller revolutions. All calculations are finished on the supercomputing system by 2 threads with 32 processers (CPU information is: Intel Xeon E5-2630 v3 × 86_64, 2.4GHz), and the calculation with the maximum mesh number spends over 2 months.

5. Results and discussion

5.1. Open water performance for HSP and CP

The experimental and numerical results for the open water performance of the HSP and CP are presented in Fig. 7 and Fig. 8. The experimental data were measured by Kurobe et al. [41]. In Fig. 7 and Fig. 8, the abscissa denotes the advance ratio, J, while the ordinate denotes the thrust coefficient, K_T, and ten times the torque coefficient, $10 K_Q$ (K_T=thrust/$\rho_l n^2 D^4$ and K_Q=torque/$\rho_l n^2 D^5$). The good agreement between the numerical and measured results shows that the current numerical methods are able to model the open water performance. In addition, the results of predicted torque coefficient at $J = 0.6$ by five meshes are shown in Fig. 9, which indicates that there is less influence on the predicted results with mesh resolution increasing.

5.2. Comparison of the measured and predicted cavitation results

The instantaneous cavitation patterns as the propeller rotating are displayed in Fig. 10 and Fig. 11 with comparisons with the measured data of Kurobe et al. [41]. The predicted cavitation shapes are visualized by the isosurface of vapor volume fraction $\alpha_v = 0.1$. Five snapshots are given for the cavitation patterns during the propeller rotating from the propeller angle $\theta = $ -10° to 70° for HSP and from $\theta = $ -30° to 50° for CP. As shown in Fig. 10 and Fig. 11, the propeller enters into a higher angle of attack region when a blade rotates into the wake defect area; thus, cavitation is then more likely to form on the propeller blade surface. The cavitation inceptions for HSP in Fig. 10 (a) and for CP
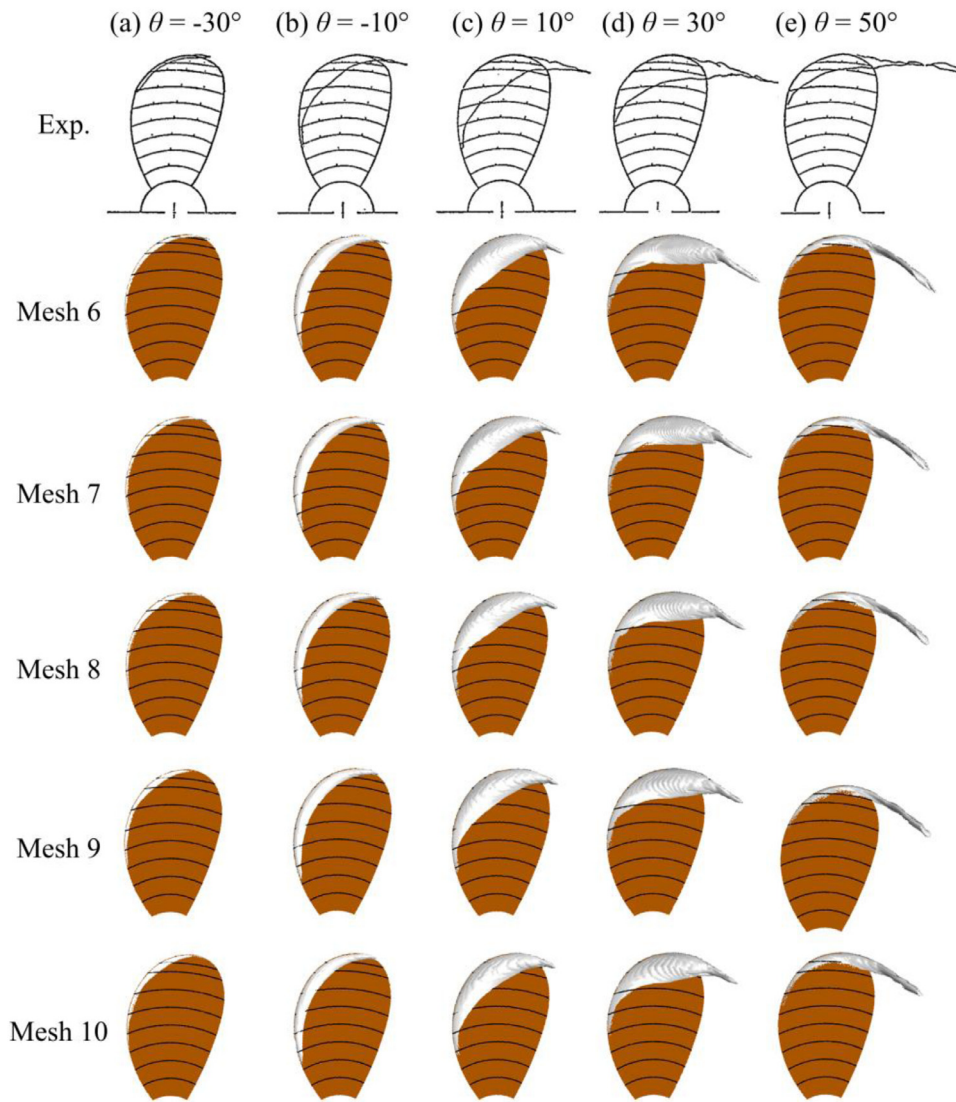
Fig. 11.. Comparison of the predicted and observed cavity patterns during propeller rotation for CP. (Experimental results [41]; predicted results: isosurface of $\alpha_v = 0.1$.)
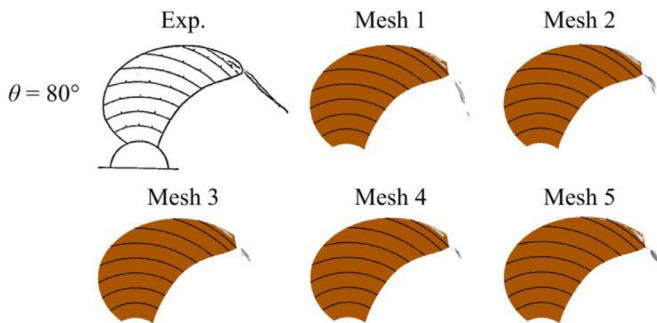

Fig. 12.. Tip vortex cavitation for HSP. (Experimental results [41]; predicted results: isosurface of $\alpha_v = 0.1$.)

Fig. 11 (a) are accurately captured by LES for all five meshes. The sheet cavitation forms from the blade leading edge, and then gradually grows over a wide blade span in the figures from part (a) to (e). Then, the sheet cavitation begins to shrink as the propeller rotates away from the wake. In the meantime, the trailing edge of the sheet cavitation grows as it is drawn into the tip vortex cavitation. Finally, the sheet cavitation almost entirely disappears as the propeller leaves the wake. The

cavitation forms later on HSP than on CP and the HPS cavitation area is smaller. In addition, the HSP sheet cavitation is more stable. The tip vortex cavitation is significantly weaker on the HSP than on the CP as shown in Fig. 12 and Fig. 13. All five meshes (Mesh 1-Mesh 5 for HSP and Mesh 6-Mesh 10 for CP) clearly show the sheet cavitation inception, development, and finally disappearance. There are only few differences in the results as the mesh resolution increases from Mesh 3 to Mesh 1 for HSP. Mesh 1 captures the best cavitation results. Similar phenomenon can be seen from Mesh 8 to Mesh 6 for CP.

The predicted and measured tip vortex cavitation for HSP and CP are compared in Fig. 12 and Fig. 13. The HSP tip vortex cavitation is weaker than that of CP. All five HSP meshes (Mesh 1 to Mesh 5) only capture a small tip vortex cavitation extent with Mesh 1 predicting a largest cavitation extent with best reproduction of the observed tip vortex cavitation than the other meshes. Fig. 13 compares the predicted tip vortex cavitation for CP with the observed cavitation. In Fig. 13 (a), the tip vortex cavitation develops from $\theta = 50°$ as shown in Fig. 11 (e) and is still very strong. As the propeller blade rotates to $\theta = 64°$ in Fig. 13 (b), the tip vortex cavitation weakens and the trailing of tip vortex cavitation becomes unstable. Finally, the trailing of tip vortex cavitation breaks down and separates from the former part of tip vortex cavitation as shown in Fig. 13 (c). The tip vortex cavitation shape in
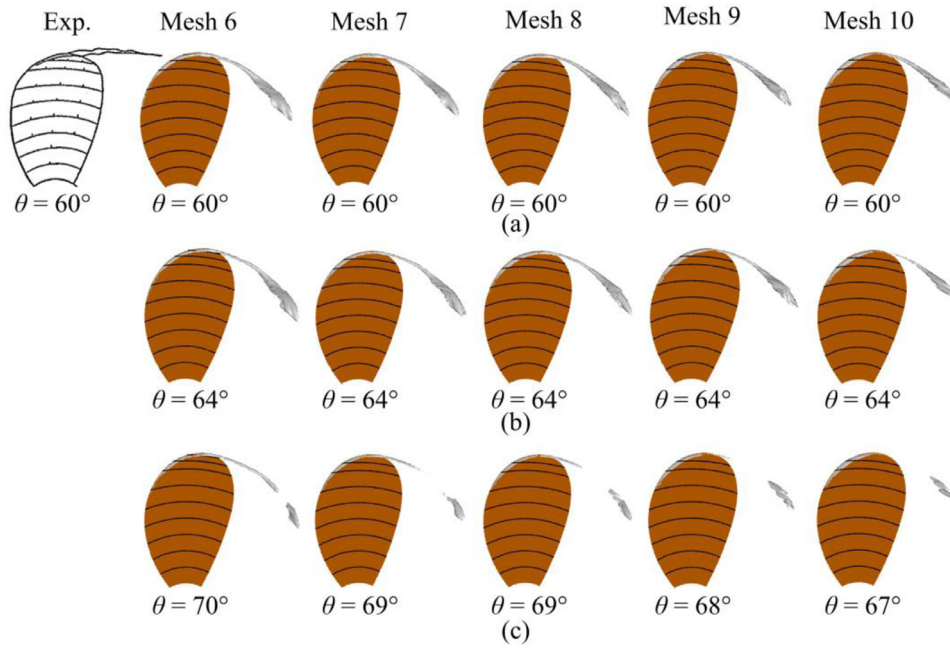
Fig. 13.. Tip vortex cavitation for CP. (a) Comparison with experimental observations at θ = 60°; (b) tip vortex cavity weakens; (c) tip vortex cavity breaks down. (Experimental results [41]; predicted results: isosurface of $\alpha_v = 0.1$.)
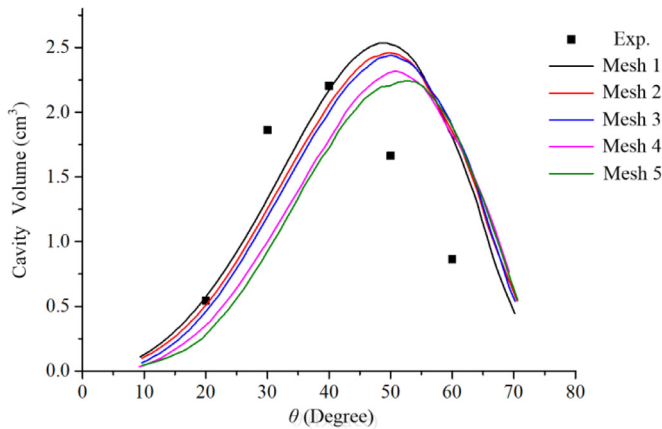

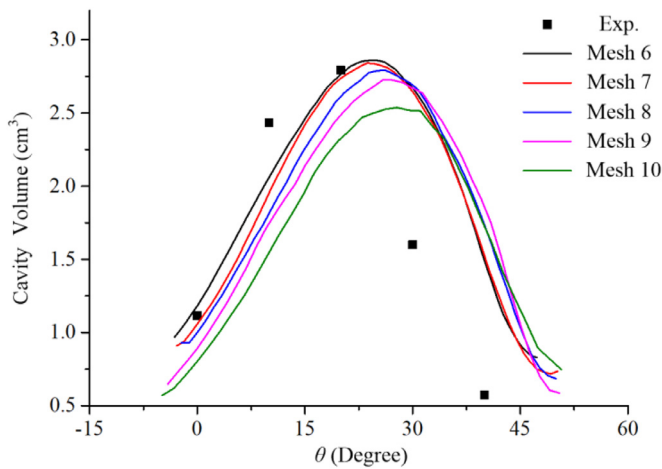**Fig. 14..** Comparison of the predicted and experimental [41] cavity volumes for HSP.

Fig. 15.. Comparison of the predicted and experimental [41] cavity volumes for CP.

Table 4.

LES errors for the average total cavity volume for HSP and CP.

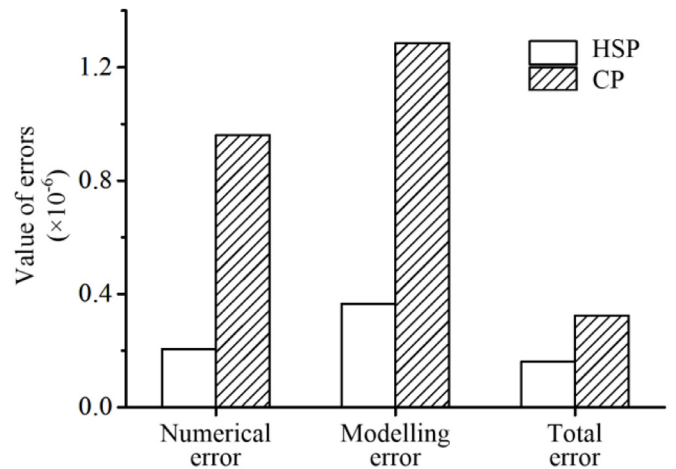| HSP	Numerical error	Modeling error	Total error
V_{cav} (× 10^{-6})	0.20465	-0.36522	-0.16057
CP	**Numerical error**	**Modeling error**	**Total error**
V_{cav} (× 10^{-6})	0.96058	-1.28484	-0.32425

Fig. 16.. Absolute values of the LES errors for the average total cavity volume for HSP and CP.

Fig. 13 (c) is different for the various mesh resolutions from Mesh 10 to Mesh 6. As the mesh resolution increases from Mesh 10 to Mesh 6, the tip vortex cavitation appears throughout larger propeller rotation ranges and the tip vortex cavitation breaks down later, e.g. $\theta = 64°$ for Mesh 10 and $\theta = 70°$ for Mesh 6 in Fig. 13 (c). The results of tip vortex cavitation in Fig. 13 show that mesh resolution larger than Mesh 8 might be able to model the shape and change of tip vortex cavitation. After examining the computational cells within the tip vortex cavitation near the blade tip for CP, it might show that at least 46 cells (cell
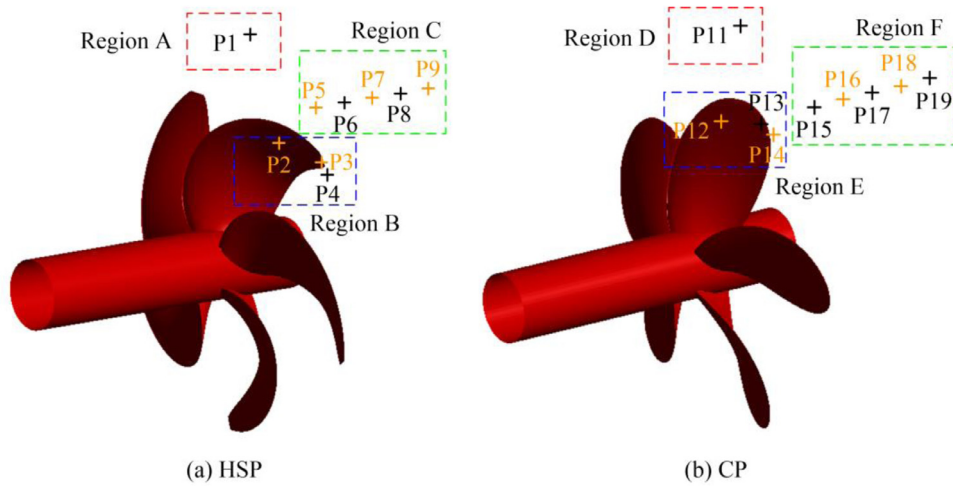
(a) HSP (b) CP

Fig. 17.. Sketch of the HSP and CP geometries and monitoring points
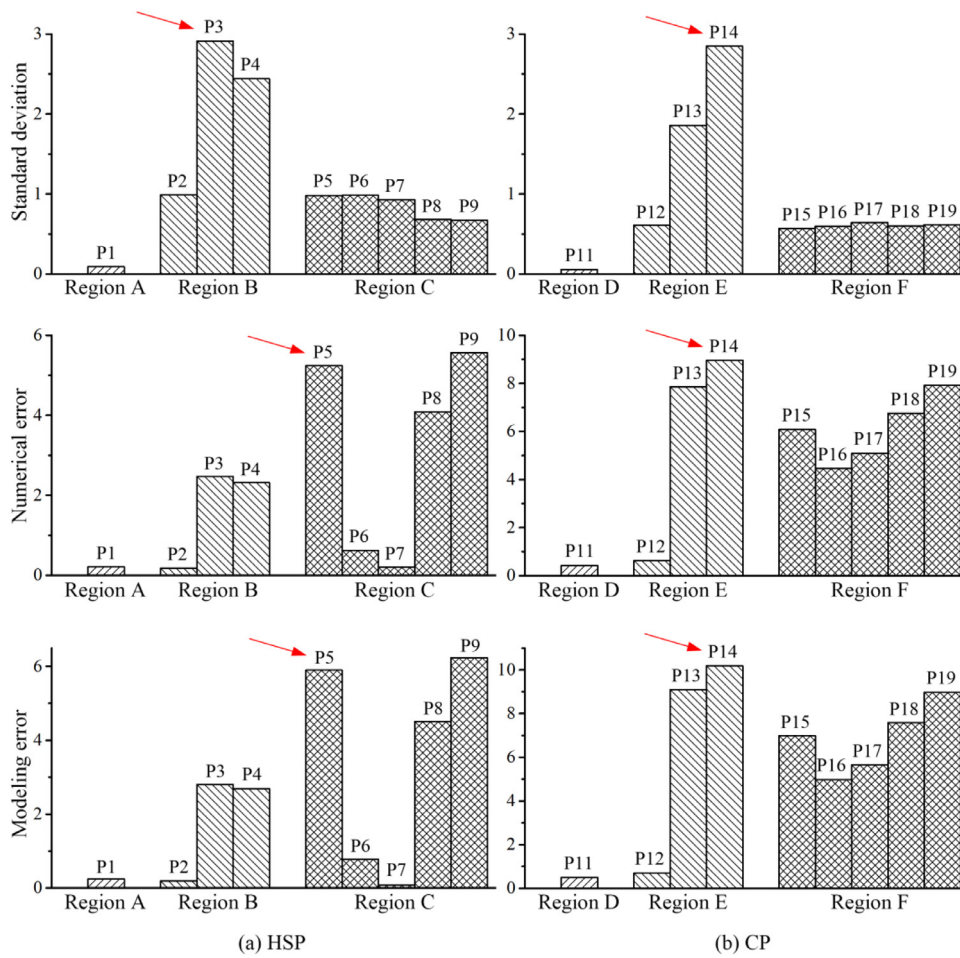

(a) HSP (b) CP

Fig. 18.. Absolute values of the errors and standard deviations for the average velocities

number of Mesh 8 within the tip vortex cavitation) are required to carry out good prediction of tip vortex cavitation on CP near the blade tip, based on the current study.

The transient extent of the sheet cavitation and the tip vortex cavitation as the propeller blade rotates are well reproduced by the current LES numerical calculations. This indicates the excellent performance prediction capability and the good calculational fidelity with the combination of the LES method and the structured mesh used in this study.

Fig. 14 and Fig. 15 compare the observed and predicted transient cavity volumes over one typical cycle as the blade goes through the wake. The main variations of the cavity volume are captured by the LES results for both HSP and CP. The predicted cavity volumes for HSP and CP both increase with increasing mesh resolution, while the propeller blade angle with the largest predicted cavity volume decreases. The results show differences between the observed and predicted volumes, which might be due to differences between the real wake in the experiments and the modeled wake in the calculations.
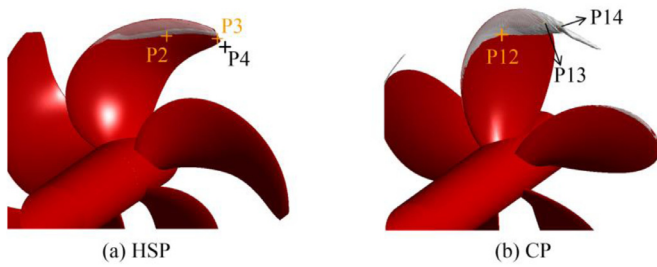
Fig. 19.. Cavitation influence on the velocity monitoring points

5.3. LES V&V results for cavitating flow around the propellers

The previous section compared the numerical results with the experimental observations, but these qualitative comparisons do not show the quantitative accuracy data. Thus, LES V&V analysis was conducted using the simplified three-equation method to demonstrate the calculational accuracy with quantitative data. It should be noted that all predicted results of cavitation pattern and vapor volume at Section 5.2 are the transient results. However, at this section, the average total vapor volume is the time average result from each instantaneous result over all propeller blades, and the average velocity is the time average result from each instantaneous result at a fixed point.

Table 4 and Fig. 16 show the LES errors of the average total cavity volume for HSP and CP. All the LES errors have been treated as absolute values in Fig. 16 for the convenience of plotting. With the current mesh topology, mesh resolution and physical model, the numerical error is slightly smaller than the modeling error for both HSP and CP. In addition, the two types of errors show opposite signs as shown in Table 4. The LES errors for the predicted average total cavity volume for HSP are smaller than those for CP. The larger skew angle for the HSP blades leads to relatively smaller cavity volume fluctuations and milder shrinkage of the cavity area from the blade hub to the tip as shown in Fig. 10 and Fig. 12. This reduces the difficulties in predicting the cavitating flow for HSP.

The influence of the cavitation on the LES errors for HSP and CP is further shown in Fig. 17–19. Fig. 17 shows the positions of the monitoring points. For HSP in Fig. 17 (a), P1 (Region A) denotes the location right above the propeller and far from the propeller influence region, P2-P4 (Region B) denote locations from the sheet cavitation to the tip vortex cavitation. P5-P9 (Region C) denote locations right behind the propeller wake. P11-P19 follow a similar distribution for CP in Fig. 17 (b). The evaluated LES errors for the average velocities for HSP and CP are shown in Fig. 18 (a) and (b) at these velocity monitoring points. The standard deviations for each velocity monitoring point are also shown which illustrates the dispersion degree of the velocity data [42]. Fig. 19 shows the influence of the cavitation on the velocities at the monitoring points for HSP and CP, and it should be noted that P13

and P14 locate in the inner cavity region.

As shown in Fig. 18 (a) for HSP, the standard deviation increases from P1 to P3, and then sharply decreases from P3 to P5. From P5 to P9, the standard deviation decreases slowly and then remains almost constant. Similar changes in the standard deviation can be seen in Fig. 18 (b) for CP with the difference being that the largest standard deviation appears at P14. These can be well explained in combination with the cavitation distributions shown from Fig. 10 to Fig. 13 and in Fig. 19. The readings at monitoring points closer to the sheet cavitation and tip vortex cavitation regions have larger standard deviations. The readings sharply decrease for monitoring points farther from the propeller, which indicates that the largest standard deviations occur in regions most influenced by the propeller cavitation (P3 in HSP and P14 in CP).

The LES error distributions are much different from the standard deviation distributions. For HSP, the LES errors increase from P1 to P3 and then decrease slightly at point P4. The peak error occurs at point P5 (the first point in Region C). For points P5-P9 in Region C, the LES errors first decrease from P5 to P7 and then increase after point P7 (the third point in Region C). The changes in the LES errors for CP can be seen in Fig. 18 (b) where the peak LES error occurs at P14 (the third point in Region E) and with the minimum error in Region F at P16 (the second point in Region F).

The signals at the monitoring points in Region B and Region E are compared with the cavity regions around the propellers in Fig. 19 to demonstrate the relationship between the LES errors and the cavity location. For the cavitation region around HSP (Region B), the error at P3 is most influenced by the sheet cavitation and the tip vortex cavitation, so the largest LES error in Region B at P3. In the cavitation region (Region E) around CP, the error at P14 is most influenced by the strong tip vortex cavitation as shown in Fig. 19, so the largest LES error in Region E occurs at P14. However, the cavitation is significantly weaker for HSP due to the larger skewed angle compared to that for CP. Propeller rotation influence on the wake becomes larger at point P5 than at P3 and P4. This leads to larger LES errors at P5 (the first point in Region C) than at P3 (second point in Region B). The dramatic sheet cavitation and long tip vortex cavitation around CP, as shown in Fig. 13 and Fig. 19, lead to the cavitation more strongly influencing the point P14 (the third point in Region E) compared to the propeller rotation influence on the near wake point P15 (the first point in Region F). So the errors are then larger at P14 with the strongest cavitation influence than at P15.

In the wake region (P5-P9 for HSP and P15-P19 for CP), the propeller influence decreases and the flow becomes more stable at the monitoring points further away from the propeller, so the LES errors decrease firstly for both HSP (P5-P7) and CP (P15-P16). However, since the mesh resolution reduces quickly in the propeller wake, the LES errors, which are influenced by the mesh resolution, gradually increase for HSP (P7-P9) and CP (P16-P19). It should be noted that this study focuses on the propeller cavitating flow, so the far propeller wake is beyond the scope of this study.
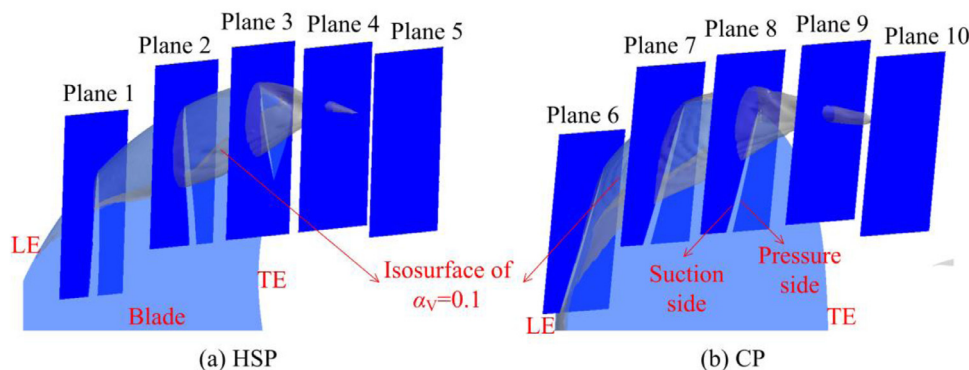

Fig. 20.. Sketch of the ten planes and locations

Fig. 21.. Predicted vapor volume fraction, *Q*-criterion, relative vorticities, and the vortex stretching, vortex dilatation, baroclinic torque and Coriolis force terms (left: HSP; right: CP)

5.4. Cavitation influences on the propeller flow structures

The last two sections show that the propeller cavitation strongly influences the local flow structures, so this section presents a detailed discussion about the effect of the propeller cavitation for HSP and CP. The instants of all figures in this section are $\theta = 50°$ and $\theta = 30°$ for HSP and CP respectively (as examples to show the cavitating flow structures around the propellers).

Fig. 20 shows the relative positions of ten selected observation planes for HSP and CP. The cavitation patterns are visualized by iso-surfaces of the vapor volume fraction and they are drawn as the transparent surfaces. The ten planes roughly correspond to the head, middle and trailing edge of the sheet cavitation region and the tip vortex cavitation region.

Fig. 21 displays the distributions of the vapor volume fraction, *Q*-criterion, relative vorticity and four terms on the right side of the relative vorticity transport equation for HSP and CP (i.e. the vortex stretching term, vortex dilatation term, baroclinic torque term and Coriolis force term. The last term is not considered due to it having little effect at high Reynolds).

Fig. 21 (a) shows the distributions of vapor volume fraction on five planes for HSP and CP respectively, and the predicted extents of the sheet cavitation and the tip vortex cavitation for CP are larger than those for HSP.

In Fig. 21 (b), the contour of *Q*-criterion contours are presented for HSP and CP. In the sheet cavitation region, the magnitude of *Q* at the liquid-vapor interface and in the cavity closure region is larger than in the other regions. For planes closer to the tip vortex cavitation, the largest *Q* is concentrated in the inner tip vortex cavitation. The evolution of the vortex structure is accompanied by change in the cavitation. The tip vortex is so strong that it is still clear even as the tip vortex cavitation disappears.

The relative vorticity distribution in Fig. 21 (c) shows that the highest vorticity is at the cavity interface at the front of the sheet cavitation. Then, large vorticities gradually concentrate on the inner sheet cavitation on the planes close to the tip vortex cavitation as shown at Fig. 21 (c) plane 8. Unlike with the *Q*-criterion, the relative vorticity decreases sharply away from the sheet cavitation on planes 4, 5, 9 and 10.

In Fig. 21 (d) and (e), the vortex stretching and dilatation term distributions show similar tendencies as the relative vorticity along the front of the sheet cavitation and in the vicinity of the tip vortex cavitation. The vortex stretching and dilatation terms are still very large near the propeller wake on planes 4 and 5 for HSP in Fig. 21 (d) and (e) and are the dominant factors influencing the vorticity transport. On planes 9 and 10 for CP in Fig. 21 (d) and (e), the region influenced by the vortex stretching and dilatation terms extends further down the propeller wake.

Fig. 21 (f) and (g) present the baroclinic torque term and Coriolis force term distributions. These two terms influence a relatively small region mainly close to the cavity closure region. The baroclinic torque has a greater effect than the Coriolis force term. The baroclinic torque term represents the vorticity generation due to misalignment of the density gradient and the pressure gradient. The Coriolis force term exists only when system is rotating. These two terms have an important influence on the vorticity generation and transport in the cavity closure region in this study, although these two terms are small. Due to the strong influence of the tip vortex cavitation for CP, all four terms are large in the inner cavitation region on plane 8 in Fig. 21 close to the tip vortex cavitation.

It shows a stripe distribution of *Q*-criterion below the tip vortex region as shown in Fig. 21 (b). This distribution is combined with the velocity vectors in Fig. 22 to study the vortical structures around the propellers. The vortical structures are plotted in Fig. 22 (b) and (c) with the *Q*-criterion isosurfaces and the velocity vector distributions on five planes. Before the tip vortex cavitation forms, the vortex is mainly at
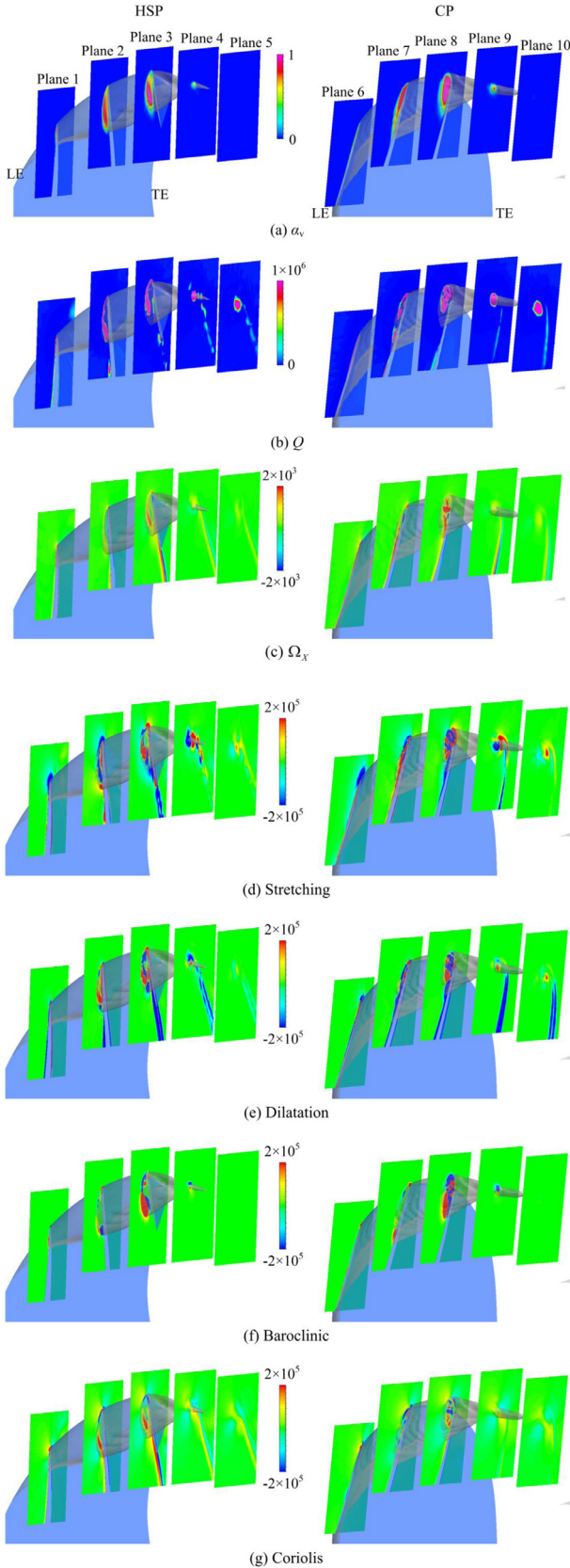
(a) Contour of Q

(b) Velocity vector and $Q = 60000$ for HSP

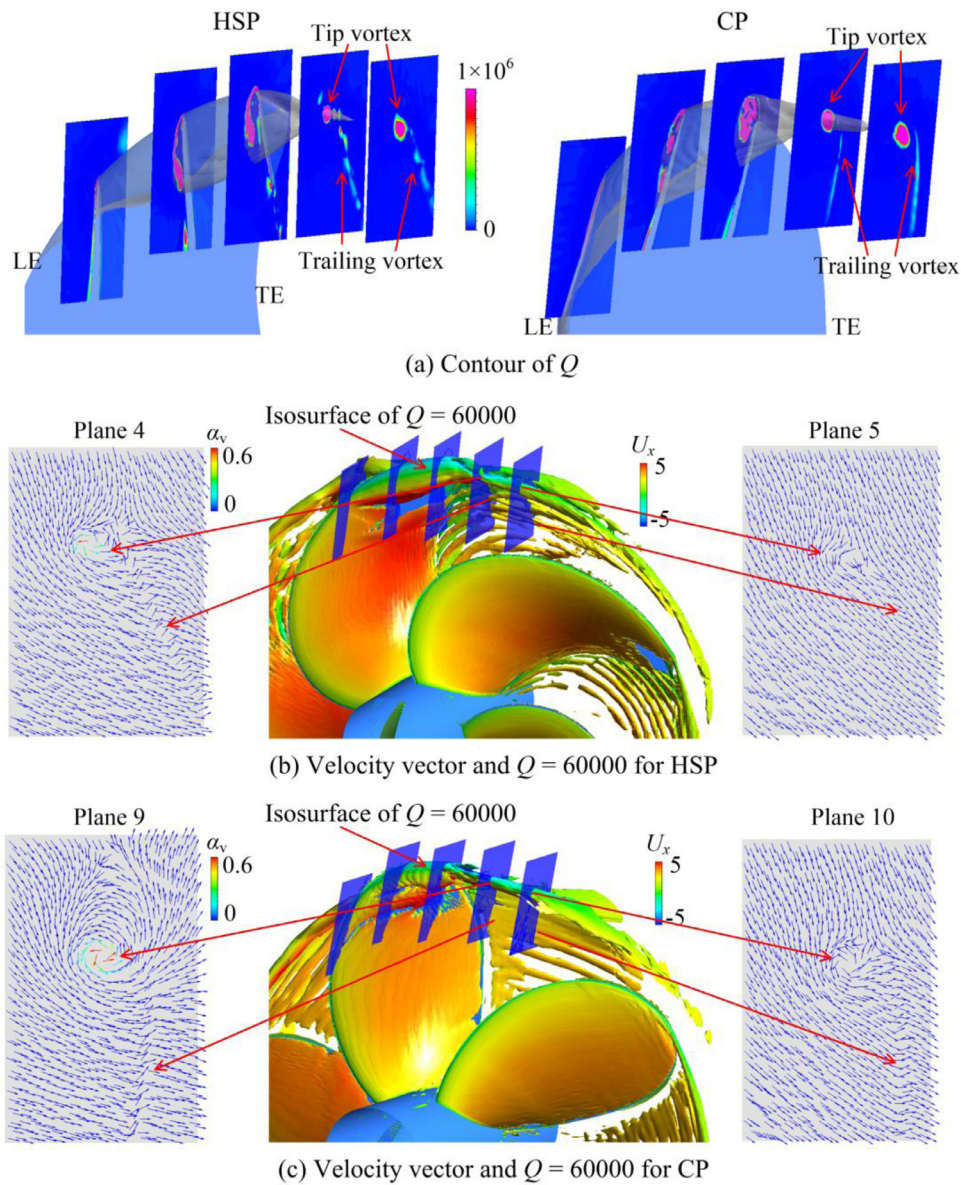(c) Velocity vector and $Q = 60000$ for CP

Fig. 22.. Vortical structures around the HSP and CP

the blade leading edge and in the cavitation region. As the flow moves away from the blade leading edge towards the propeller wake, the leading edge vortex rolls into the strong tip vortex with the tip vortex cavitation forming. The pressure decreases to a very low level in the tip vortex and the cavitation easily forms in the vortex tube as shown in Fig. 22 (b) plane 4 and Fig. 22 (c) plane 9.

The tip vortex identified by the velocity vector strongly influences and changes the local flow directions. The striped Q-criterion distribution in Fig. 22 (a) corresponds to the trailing vortices, which are also indicated by the velocity vectors in Fig. 22 (b) and (c). These trailing vortices are much weaker than the tip vortex, but they still change the local flow direction as shown in planes 4 and 9. As the observed position moves away from the blade tip as shown in planes 5 and 10, the tip vortex and the trailing vortex rapidly become weaker while the vortical structures are still stronger for CP in plane 10 than for HSP in plane 5.

The re-entrant jet has been shown to be one of the main mechanisms leading to the cloud cavitation around hydrofoils by many researchers [1,2,15]. Fig. 23 shows velocity fields that illustrate the re-entrant flow in the propeller cavitation. Fig. 23 shows the radial velocity distribution

and velocity vectors near the cavitation to show the detailed cavitating flow around the propeller. The side-entrant jet appears underneath the cavity surface. As the flow moves towards the blade trailing edge, the sheet cavitation becomes thicker and is lifted up from the blade surface by the side-entrant jet. Then, the sheet cavitation gradually rolls up and is finally drawn into the tip vortex cavitation. The highly skewed HSP geometry causes part of the sheet cavitation to remain attached to the blade surface from the leading edge to the trailing edge even with the influence of the side-entrant jet. The sheet cavitation on CP pulls away from the blade surface very early along the blade to form a large vortex core. Then, much vapor is drawn into the tip vortex cavitation. The strong tip vortex cavitation on CP shown in Fig. 23 seriously affects the machine safety.

6. Conclusions

LES was coupled with a homogenous cavitation model to simulate turbulent cavitating flow around conventional and highly skewed marine propellers with emphasis on the skew angle effects. LES V&V was used in the propeller cavitation with the simplified three-equation
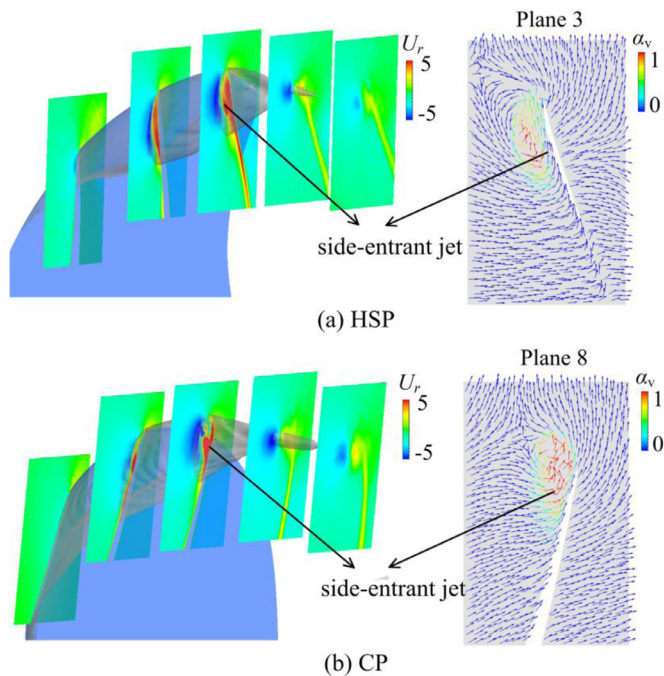
Fig. 23.. Radial velocity distribution and velocity vectors around the HSP and CP

method. The results were used to study the cavitation influence on the flow structures around the propellers. The tip vortex, leading edge vortex, trailing vortex and internal jet were identified in the current simulations. The main conclusions can be summarized as,

(1) LES can accurately predict the complex cavitating flow around the HSP and CP, including the sheet cavitation and the tip vortex cavitation. The transient evolution of the cavity patterns and cavity volume are accurately reproduced by the LES model with the results in good agreement with experimental observations. Thus, this numerical methodology, including the structured meshes, LES method, and mass transfer model, is able to simulate the transient propeller cavitating flow.

(2) The LES errors are significantly influenced by the unsteady cavitation around the propeller. The LES errors for the average cavity volume and the average velocity for CP are clearly larger than for HSP. The relatively smaller cavity volume fluctuations and milder shrinkage of cavity area around HSP due to more skewed blade reduces the difficultly of numerical prediction. The larger skew angle then may leads to higher calculational accuracy for HSP than for CP with similar numerical methods and mesh topologies.

(3) The results also show the influence of the propeller cavitation on the vorticity distribution and transport. In front of the sheet cavitation, the vorticity is mainly located in the inner tip vortex cavitation and at the cavity interface. The vortex stretching and dilatation terms are larger in front of the sheet cavitation and near the tip vortex cavitation region. The baroclinic torque term and the Coriolis force term are larger in the cavity closure region where they have a large influence on the vorticity generation and transport.

(4) The tip vortex, leading edge vortex, trailing vortex and internal jet are clearly identified in the current LES simulations. The tip vortex and the trailing vortex influence the propeller wake flow. The strong side-entrant jet is clearly seen for CP, while the effect of the side-entrant jet is much smaller around HSP due to the highly skewed blade. In addition, the CP has significantly more intense and violent vortical structures and cavitation phenomena than the HSP.

CRediT authorship contribution statement

Yun Long: Software, Validation, Investigation, Data curation, Writing - original draft. **Chengzao Han:** Software, Validation, Investigation, Data curation, Writing - original draft. **Bin Ji:** Resources, Writing - review & editing, Supervision, Project administration, Funding acquisition. **Xinping Long:** Conceptualization, Methodology, Writing - review & editing. **Yiwei Wang:** Writing - review & editing.

Declaration of Competing Interests

The authors declare that they have no known competing financial interests or personal relationships that could have appeared to influence the work reported in this paper.

Supplementary materials

Supplementary material associated with this article can be found, in the online version, at doi:10.1016/j.apor.2020.102167.

References

[1] H.Y. Cheng, X.R. Bai, X.P. Long, B. Ji, X.X. Peng, M. Farhat, Large eddy simulation of the tip-leakage cavitating flow with an insight on how cavitation influences vorticity and turbulence, Appl. Math. Model. 77 (2020) 788–809.

[2] B. Huang, S.C. Qiu, X.B. Li, Q. Wu, G.Y. Wang, A review of transient flow structure and unsteady mechanism of cavitating flow, J. Hydrodyn. Ser. B 31 (3) (2019) 429–444.

[3] C.Z. Han, Y. Long, B. Ji, X.P. Long, Z.R. Zhang, An integral calculation approach for numerical simulation of cavitating flow around a marine propeller behind the ship hull, J. Hydrodyn. Ser. B 30 (6) (2018) 1186–1189.

[4] A.P. Francisco, D.F. Fabio, S. Francesco, Propeller cavitation in non-uniform flow and correlation with the near pressure field, J. Mar. Sci. E 4 (4) (2016) 70.

[5] S.H. Rhee, T. Kawamura, H. Li, Propeller cavitation study using an unstructured grid based Navier-Stoker solver, ASME J. Fluids Eng. 127 (5) (2005) 986–994.

[6] K. Takashi, A. Jun, Numerical analysis of steady and unsteady sheet cavitation on a marine propeller using a simple surface panel method "SQCM", First International Symposium on Marine Propulsors, Trondheim, Norway, 2009.

[7] J.W. Lindau, D.A. Boger, R.B. Medvitz, R.F. Kunz, Propeller cavitation breakdown analysis, ASME J. Fluids Eng. 127 (5) (2005) 995–1002.

[8] B. Ji, X.W. Luo, X.X. Peng, Y.L. Wu, H.Y. Xu, Numerical analysis of cavitation evolution and excited pressure fluctuation around a propeller in non-uniform wake, Int. J. Multiphase Flow 43 (43) (2012) 13–21.

[9] B. Ji, X.W. Luo, Y.L. Wu, X.X. Peng, H.Y. Xu, Partially-averaged Navier–Stokes method with modified k–ε model for cavitating flow around a marine propeller in a non-uniform wake, Int. J. Heat Mass Transfer 55 (23–24) (2012) 6582–6588.

[10] B. Ji, X.W. Luo, X. Wang, X.X. Peng, Y.L. Wu, H.Y. Xu, Unsteady numerical simulation of cavitating turbulent flow around a highly skewed model marine propeller, ASME J. Fluids Eng. 133 (1) (2011) 011102.

[11] P.B. Regener, Y. Mirsadraee, P. Andersen, Nominal vs. effective wake fields and their influence on propeller cavitation performance, J. Mar. Sci. E 6 (2) (2018) 34.

[12] M. Morgut, E. Nobile, Influence of the mass transfer model on the numerical prediction of the cavitating flow around a marine propeller, Second International Symposium on Marine Propulsors, Hamburg, Germany, 2011.

[13] K. Sato, A. Oshima, H. Egashira, S. Takano, Numerical prediction of cavitation and pressure fluctuation around marine propeller, The 7th International Symposium on Cavitation, Michigan, USA, 2009.

[14] Q. Wu, B. Huang, G. Wang, S. Cao, M. Zhu, Numerical modelling of unsteady cavitation and induced noise around a marine propeller, Ocean Eng. 160 (2018) 143–155.

[15] Y. Long, X.P. Long, B. Ji, T. Xing, Verification and validation of large eddy simulation of attached cavitating flow around a Clark-Y hydrofoil, Int. J. Multiphase Flow 115 (2019) 93–107.

[16] A. Sou, B. Biçer, A. Tomiyama, Numerical simulation of incipient cavitation flow in a nozzle of fuel injector, Comput. Fluids 103 (2014) 42–48.

[17] R. Bensow, G.r. Bark, Implicit LES predictions of the cavitating flow on a propeller, ASME J. Fluids Eng. 132 (4) (2010) 041302.

[18] R.E. Bensow, G.r. Bark, Simulating cavitating flows with LES in openfoam, in: J.C.F. Pereira, A. Sequeira (Eds.), Fifth European Conference on Computational Fluid Dynamics, Lisbon, Portugal, 2010.

[19] N.X. Lu, U. Svennberg, G.r. Bark, R.E. Bensow, Numerical simulations of the cavitating flow on a marine propeller, in: OHL Claus-Dieter (Ed.), 8th International Symposium on Cavitation, Singapore, 2012.

[20] N.X. Lu, R.E. Bensow, G. Bark, Large eddy simulation of cavitation development on highly skewed propellers, J. Mar. Sci. Technol. 19 (2) (2014) 197–214.

[21] C. Yu, Y. Wang, C. Huang, X. Wu, T. Du, Large eddy simulation of unsteady cavitating flow around a highly skewed propeller in nonuniform wake, ASME J. Fluids Eng. 139 (4) (2017) 041302.

[22] P.J. Roache, Verification and Validation in Computational Science and Engineering, Hermosa, Albuquerque, NM, 1998.

[23] W.L. Oberkampf, C.J. Roy, Verification and Validation in Scientific Computing, Cambridge University Press, 2010.

[24] M. Freitag, M. Klein, An improved method to assess the quality of large eddy simulations in the context of implicit filtering, J. Turbul. 7 (2006) 1–11.

[25] M. Klein, An attempt to assess the quality of large eddy simulations in the context of implicit filtering, Flow Turbul. Combust. 75 (1–4) (2005) 131–147.

[26] T. Xing, A general framework for verification and validation of large eddy simulations, J. Hydrodyn. Ser. B 27 (2) (2015) 163–175.

[27] R. Dutta, T. Xing, Quantitative solution verification of large eddy simulation of channel flow, the 2nd Thermal and Fluid Engineering Conference, Las Vegas, NV, USA, 2017.

[28] R. Dutta, T. Xing, Five-equation and robust three-equation method for solution verification of large eddy simulations, J. Hydrodyn. Ser. B 30 (1) (2018) 23–33.

[29] X.P. Long, Y. Long, W. Wang, H.Y. Cheng, B. Ji, Some notes on numerical simulation and error analyses of the attached turbulent cavitating flow by LES, J. Hydrodyn. Ser. B 30 (2) (2018) 369–372.

[30] J.S. Smagorinsky, General circulation experiments with the primitive equations, Mon. Weather Rev. 91 (3) (1963) 99–164.

[31] A. Hadjadj, O. Bennasr, M.S. Shadloo, A. Chaudhuri, Effect of wall temperature in supersonic turbulent boundary layers: a numerical study, Int. J. Heat Mass Transfer 81 (2015) 426–438.

[32] O. Ben-Nasr, A. Hadjadj, A. Chaudhuri, M.S. Shadloo, Assessment of subgrid-scale modeling for large-eddy simulation of a spatially-evolving compressible turbulent boundary layer, Comput. Fluids 151 (2017) 144–158.

[33] M. Rieth, F. Proch, O.T. Stein, M.W.A. Pettit, A.M. Kempf, Comparison of the Sigma and Smagorinsky LES models for grid generated turbulence and a channel flow, Comput. Fluids 99 (2014) 172–181.

[34] A. Ducoin, M.S. Shadloo, S. Roy, Direct Numerical Simulation of flow instabilities over Savonius style wind turbine blades, Renewable Energy 105 (2017) 374–385.

[35] F.J. Salvador, J. Martínez-López, J.-V. Romero, M.-D. Roselló, Computational study of the cavitation phenomenon and its interaction with the turbulence developed in diesel injector nozzles by large eddy simulation (LES), Math. Comput. Model. 57 (2013) 1656–1662.

[36] G.H. Schnerr, J. Sauer, Physical and numerical modeling of unsteady cavitation dynamics, ICMF 2001 4th International Conference on Multiphase Flow, New Orleans, USA, 2001.

[37] A.K. Singhal, M.M. Athavale, H. Li, Y. Jiang, Mathematical basis and validation of the full cavitation model, ASME J. Fluids Eng. 124 (3) (2002) 617–624.

[38] P.J. Zwart, A.G. Gerber, T. Belamri, A two-phase flow model for predicting cavitation dynamics, ICMF 2004 International Conference on Multiphase Flow, Yokohama, Japan, 2004.

[39] Y. Long, X.P. Long, B. Ji, H. Huang, Numerical simulations of cavitating turbulent flow around a marine propeller behind the hull with analyses of the vorticity distribution and particle tracks, Ocean Eng. 189 (2019) 106310.

[40] B. Huang, Y. Young L, G. Wang, S. Wei, Combined experimental and computational investigation of unsteady structure of sheet/cloud cavitation, ASME J. Fluids Eng. 135 (7) (2013) 071301.

[41] Kurobe, Y., Ukon, Y., Koyama, K., Masahiko, M., Measurement of Cavity Volume and Pressure Fluctuations on a Model of the Traininng Ship Seiun-Maru with Reference to Full Scale Measurement, Ship Research Institute, Technique Report No (NAID) 110007663078, 1983.

[42] J. Wang, L. Wang, S. Xu, B. Ji, X.P. Long, Experimental investigation on the cavitation performance in a venturi reactor with special emphasis on the choking flow, Exp. Therm. Fluid Sci. 106 (2019) 215–225.